Research Article Vol. 25, No. 18 | 4 Sep 2017 | OPTICS EXPRESS 21321

Optics EXPRESS

Depth resolved snapshot energy-dispersive X-ray diffraction using a conical shell beam

A. J. DICKEN,[1] J. P. O. EVANS,[1,*] K. D. ROGERS,[2] D. PROKOPIOU,[2] S. X. GODBER,[3] AND M. WILSON[4]

[1] *Imaging Science Group, Rosalind Franklin Building, Clifton, Nottingham Trent University, Nottingham, UK*
[2] *Cranfield Forensic Institute, Cranfield University, Shrivenham, Swindon, UK*
[3] *Halo X-ray Technologies, BioCity, Nottingham, UK*
[4] *Detector Development Group, Rutherford Appleton Laboratory, Didcot, UK*
[*] *paul.evans@ntu.ac.uk*

Abstract: We demonstrate a novel imaging architecture to collect range encoded diffraction patterns from overlapping samples in a single conical shell projection. The patterns were measured in the dark area encompassed by the beam via a centrally positioned aperture optically coupled to a pixelated energy-resolving detector. We show that a single exposure measurement of 0.3 mAs enables d-spacing values to be calculated. The axial positions of the samples were not required and the resultant measurements were robust in the presence of crystallographic textures. Our results demonstrate rapid volumetric materials characterization and the potential for a direct imaging method, which is of great relevance to applications in medicine, non-destructive testing and security screening.

OCIS codes: (110.7440) X-ray imaging; (110.6955) Tomographic imaging; (340.7430) X-ray coded apertures; (110.3200) Inverse scattering.

References and links

1. W. C. Röntgen, "On a new kind of rays," Science **3**(59), 227–231 (1896).
2. S. A. Zhou and A. Brahme, "Development of phase-contrast X-ray imaging techniques and potential medical applications," Phys. Med. **24**(3), 129–148 (2008).
3. S. Huotari, T. Pylkkänen, R. Verbeni, G. Monaco, and K. Hämäläinen, "Direct tomography with chemical-bond contrast," Nat. Mater. **10**(7), 489–493 (2011).
4. G. Harding, H. Fleckenstein, D. Kosciesza, S. Olesinski, H. Strecker, T. Theedt, and G. Zienert, "X-ray diffraction imaging with the multiple inverse fan beam topology: Principles, performance and potential for security screening," Appl. Radiat. Isot. **70**(7), 1228–1237 (2012).
5. K. MacCabe, K. Krishnamurthy, A. Chawla, D. Marks, E. Samei, and D. Brady, "Pencil beam coded aperture x-ray scatter imaging," Opt. Express **20**(15), 16310–16320 (2012).
6. J. A. Greenberg, K. Krishnamurthy, and D. Brady, "Snapshot molecular imaging using coded energy-sensitive detection," Opt. Express **21**(21), 25480–25491 (2013).
7. C. Hall, S. L. Colston, A. C. Jupe, S. D. M. Jacques, R. Livingston, A. O. A. Ramadan, A. W. Made, and P. Barnes, "Non-destructive tomographic energy-dispersive diffraction imaging of the interior of bulk concrete," Cement Concr. Res. **30**(3), 491–495 (2000).
8. A. M. Beale, S. D. M. Jacques, E. K. Gibson, and M. D. Michiel, "Progress towards five dimensional diffraction imaging of functional materials under process conditions," Coord. Chem. Rev. **277–278**, 208–223 (2014).
9. D. O'Flynn, C. B. Reid, C. Christodoulou, M. D. Wilson, M. C. Veale, P. Seller, D. Hills, H. Desai, B. Wong, and R. Speller, "Explosive detection using pixelated X-ray diffraction (PixD)," JINST **8**, P03007 (2013).
10. D. O'Flynn, H. Desai, C. B. Reid, C. Christodoulou, M. D. Wilson, M. C. Veale, P. Seller, D. Hills, B. Wong, and R. D. Speller, "Identification of simulants for explosives using pixelated X-ray diffraction," Crime Sci. **2**, 4 (2013).
11. D. O'Flynn, C. Crews, I. Drakos, C. Christodoulou, M. D. Wilson, M. C. Veale, P. Seller, and R. D. Speller, "Materials identification using a small-scale pixelated x-ray diffraction system," J. Phys. D Appl. Phys. **49**(17), 175304 (2016).
12. J. Greenberg, K. Krishnamurthy, and D. Brady, "Compressive single-pixel snapshot x-ray diffraction imaging," Opt. Lett. **39**(1), 111–114 (2014).
13. K. P. MacCabe, A. D. Holmgren, M. P. Tornai, and D. J. Brady, "Snapshot 2D tomography via coded aperture x-ray scatter imaging," Appl. Opt. **52**(19), 4582–4589 (2013).
14. S. Pang, M. Hassan, J. Greenberg, A. Holmgren, K. Krishnamurthy, and D. Brady, "Complementary coded apertures for 4-dimensional x-ray coherent scatter imaging," Opt. Express **22**(19), 22925–22936 (2014).

#301314 https://doi.org/10.1364/OE.25.021321
Journal © 2017 Received 29 Jun 2017; revised 16 Aug 2017; accepted 18 Aug 2017; published 23 Aug 2017

15. J. A. Greenberg, M. Hassan, K. Krishnamurthy, and D. Brady, “Structured illumination for tomographic X-ray diffraction imaging,” Analyst (Lond.) **139**(4), 709–713 (2014).
16. P. Evans, K. Rogers, J. Chan, J. Rogers, and A. Dicken, “High intensity X-ray diffraction in transmission mode employing an analog of Poisson’s spot,” Appl. Phys. Lett. **97**(20), 204101 (2010).
17. A. Dicken, A. Shevchuk, K. Rogers, S. Godber, and P. Evans, “High energy transmission annular beam X-ray diffraction,” Opt. Express **23**(5), 6304–6312 (2015).
18. A. J. Dicken, J. P. O. Evans, K. D. Rogers, C. Greenwood, S. X. Godber, D. Prokopiou, N. Stone, J. G. Clement, I. Lyburn, R. M. Martin, and P. Zioupos, “Energy-dispersive X-ray diffraction using an annular beam,” Opt. Express **23**(10), 13443–13454 (2015).
19. D. Prokopiou, K. Rogers, P. Evans, S. Godber, and A. Dicken, “Discrimination of liquids by focal construct technology,” Appl. Radiat. Isot. **77**, 160–165 (2013).
20. K. Rogers, P. Evans, J. Rogers, J. Chan, and A. Dicken, “Focal construct geometry – a novel approach to the acquisition of diffraction data,” J. Appl. Cryst. **43**(2), 264–268 (2010).
21. J. P. O. Evans, S. X. Godber, F. Elarnaut, D. Downes, A. J. Dicken, and K. D. Rogers, “X-ray absorption tomography employing a conical shell beam,” Opt. Express **24**(25), 29048–29059 (2016).
22. P. Evans, K. Rogers, A. Dicken, S. Godber, and D. Prokopiou, “X-ray diffraction tomography employing an annular beam,” Opt. Express **22**(10), 11930–11944 (2014).
23. D. Prokopiou, K. L. Smith, K. Rogers, P. Paula, P. Evans, A. Dicken, and S. Godber, “Simulations and experimental demonstrations of encoding for X-ray coherent scattering,” J. Appl. Cryst. **50**(2), 411–418 (2017).
24. P. Seller, S. Bell, R. J. Cernik, C. Christodoulou, C. K. Egan, J. A. Gaskin, S. Jacques, S. Pani, B. D. Ramsey, C. Reid, P. J. Sellin, J. W. Scuffham, R. D. Speller, M. D. Wilson, and M. C. Veale, “Pixellated Cd(Zn)Te high-energy X-ray instrument,” J. Instrum. **6**(12), C12009 (2011).
25. B. Ghammraoui, V. Rebuffel, J. Tabary, C. Paulus, L. Verger, and P. Duvauchelle, “Effect of grain size on stability of X-ray diffraction patterns used for threat detection,” Nucl. Instrum. Methods Phys. Res. A **683**, 1–7 (2012).
26. R. D. Luggar, J. A. Horrocks, R. D. Speller, and R. J. Lacey, “Determination of the geometric blurring of an energy dispersive X-ray diffraction (EDXRD) system and its use in the simulation of experimentally derived diffraction profiles,” Nucl. Instrum. Methods Phys. Res. **383**(2-3), 610–618 (1996).
27. K. Rogers, S. E. Etok, and R. Scott, “Structural characterisation of apatite coatings,” J. Mater. Sci. **39**(18), 5747–5754 (2004).
28. S. J. Chipera and D. L. Bish, “Fitting full X-ray diffraction patterns for quantitative analysis: a method for readily quantifying crystalline and disordered phases,” Adv. in Mater. Phys. and Chem. **3**, 47–53 (2013).
29. J. Rius, F. Plana, and A. Palanques, “A standardless X-ray diffraction method for the quantitative analysis of multiphase mixtures,” J. Appl. Cryst. **20**(6), 457–460 (1987).
30. C. V. Pabón, P. Frutos, J. L. Lastres, and G. Frutos, “Application of differential scanning calorimetry and X-ray powder diffraction to the solid-state study of metoclopramide,” J. Pharm. Biomed. Anal. **15**(1), 131–138 (1996).

1. Introduction

There is a growing requirement to provide high speed, non-invasive materials characterization of complex heterogeneous objects in fields as diverse as materials science, medicine and security screening. X-rays offer the potential for penetrative inspection to be combined with structural characterization via their coherent interaction with the spatial distribution of electrons in the objects under inspection [1]. Analytical imaging techniques employing X-rays include computerized tomography (CT), phase contrast [2], X-ray spectroscopy [3] and X-ray diffraction (XRD) [4,5]. XRD is capable of providing material-specific signatures through optically long specimen paths [6]. Classically, atomic scale (and greater) periodicities within a sample result in constructive interference of elastically scattered X-rays with a characteristic energy-angle relationship. This relationship is well understood and described by Bragg’s condition $d = n\lambda/2\sin\theta$, where d is the material inter-planar spacing or periodicity, λ is the incident photon wavelength, 2θ is the angle through which photons are coherently scattered with respect to the primary beam, and higher-order diffraction is modelled by the integer n. Traditionally, there are two different methods of implementing X-ray diffraction within analytical instruments. Angular-dispersive X-ray diffraction (ADXRD) employs a monochromatic incident beam and measures the intensity of coherent scatter from a sample over an operational angular range. While energy-dispersive X-ray diffraction (EDXRD) employs a broadband interrogating beam of radiation to measure the energy or wavelength, via the Planck-Einstein relation, of coherent scatter at a fixed angle. Both approaches employ identical physical principles to enable the calculation of d-spacing values but require quite different physical implementations. Examples of each method have been adapted for analytical imaging [7,8]. In the case of ADXRD spectral modification, i.e. monochromatization of the beam is required while in EDXRD spatial encoding or angular acceptance windowing [6] is necessary. Many potential applications requiring material phase identification are time critical. For example, X-ray screening of luggage in aviation security applications provides around 5 seconds for the inspection of a bag at a security checkpoint. However, it is worth noting that ‘typically’ <<1% of the primary beam is coherently scattered by a polycrystalline material. Consequently, the amount of diffracted flux available from a given gauge volume may be orders of magnitude smaller in comparison with the corresponding absorption contrast flux i.e. the image forming signals in radiography. A conventional approach to the collection of diffracted flux will require significantly longer integration times and or brighter X-ray sources in comparison to conventional mass absorption imaging. This temporal aspect is exacerbated by the reduction in coherent scattering cross sections or probability of interaction at the X-ray energies e.g. ~140 keV employed routinely within the aviation X-ray security industry for the inspection of checked luggage [4]. In response to this problem hybrid XRD systems, measuring broadband diffracted flux over a relatively large angular range, are showing great promise. Some of these methods require *a priori* knowledge of sample position [9–11] while others accommodate unknown sample positions within an inspection volume [6, 12–15].

2. Methods

2.1 Theory background

Focal construct geometry (FCG) refers to an alternate X-ray beam topology designed to reduce the exposure time required for the collection and analysis of Bragg scatter from samples. A conical shell beam of radiation provides an extended specimen path that increases the number of crystallites in the correct orientation to produce relatively high intensity focal spots [16] and caustics in the diffracted flux [17]. This beam topology has been implemented successfully in energy [18] and angular dispersive modes [19–21], used to identify liquid samples [19], and shown to deal favorably with non-ideal samples in which scattering distributions are adversely affected by crystallographic textures e.g. preferred orientation and large grain size [20]. In addition, annular projections collected over a two-axis raster scan can optically encode the shape and location of object features along the beam to provide the basis for absorption contrast tomography [21], and angular-dispersive tomography [22]. An angular-dispersive method employing spiral or linear post sample occluders [23] to provide depth encoding has also been implemented although this method does not collect spatial images.

2.2 New system architecture

In contrast to previous FCG single projection techniques, no *a priori* positional information is required to compute d-spacings from samples positioned within a polychromatic conical shell beam. A single spatially resolved snapshot image encodes source-to-sample distance z and associated 2θ values. Thus, the novelty of our snapshot ED FCG method lies within the geometry of the system architecture presented in Fig. 1. A pinhole aperture is positioned along the symmetry axis of the system to receive diffracted flux from samples within the beam. Each annular gauge volume is imaged (simultaneously) as a range dependent characteristic polychromatic ring with a pixelated energy-resolving detector.

To establish the relationship between d-spacings and spatially resolved spectral measurements we consider normally positioned samples as shown in Fig. 1. An annular gauge volume is subtended by the maximum and minimum half-opening angles of the primary beam envelope ϕ_{max} and ϕ_{min}, respectively. The spot size of the X-ray source is considered negligible. Conical shells of diffracted flux from axial positions, z along the gauge volume propagate through a circular aperture of radius, a, at distance, A from the X-ray point source. The resultant angular distribution of the diffracted beam is bounded by a maximum, $2\theta_{\max}$, and a minimum, $2\theta_{\min}$, value according to

$$2\theta_{\max,\min} = \tan^{-1}\left[\frac{\pm a + z_{\max,\min}\tan\phi_{\max,\min}}{A - z_{\max,\min}}\right] + \phi_{\max,\min}, \tag{1}$$

where the angular spread of the primary beam about a mean angle ϕ is given by, $\Delta\phi = \phi_{\max} - \phi_{\min}$. A nominal 2θ value for a given axial position z is obtained by setting; a=0, $\phi_{\max} = \phi_{\min} = \phi$ in Eq. (1). Under these hypothetical conditions the diffracted rays from an axial plane form a point projection of a circular conic section upon the detection plane. The separation between the detector and aperture is specified as a focal length $f = D - A$, as shown in Fig. 1.

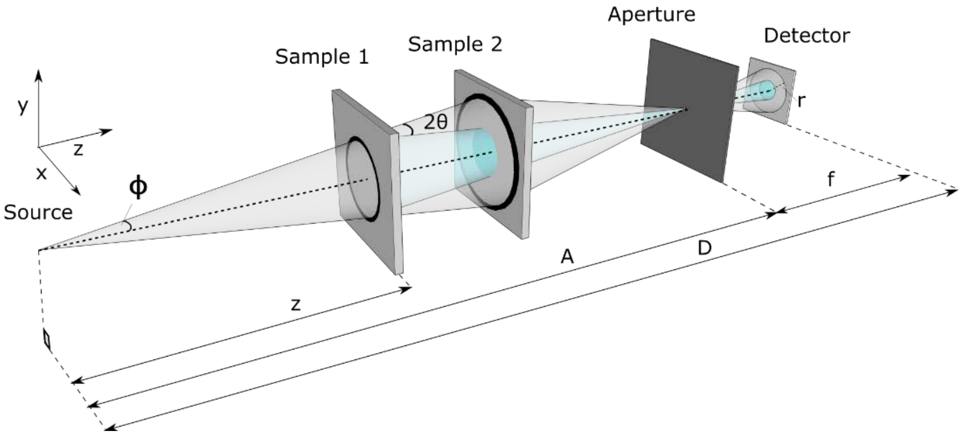

Fig. 1. Coordinate system diagram illustrating a conical shell X-ray beam incident upon two planar samples at different (unknown) ranges. The diffracted flux from the samples is focused via the aperture into characteristic depth dependent radii on a pixelated energy resolving detector.

The source-to-sample separation is given by

$$z = \frac{Ar}{r + f\tan\phi}. \tag{2}$$

An estimate of d-spacing values may be calculated as a function of the dependent variables, $f(r,\lambda)$ by substituting for θ in Bragg's condition to give

$$d = \frac{n\lambda}{2\sin\left\{\frac{1}{2}\left[\tan^{-1}\left(\frac{r}{f}\right) + \phi\right]\right\}}. \tag{3}$$

It can be appreciated from Eq. (1) that the practical requirement for a finite aperture, a, and primary beam envelope $\Delta\phi$, produce a spread in diffraction angle, $\Delta 2\theta = 2\theta_{\max} - 2\theta_{\min}$ such that a range of wavelengths satisfy Bragg's condition for a given d-spacing. The corresponding first order spread in spectral energy may be expressed as;

$E_{\max/\min} = 6.2 / d \sin\theta_{\min/\max}\,(\text{keV})$ where d (Å). The effect of geometric broadening upon the calculated d-spacing values, $\Delta d = d_{\max} - d_{\min}$ may be estimated from

$$\mathrm{d}_{\min/\max} = \frac{\mathrm{hc}}{2\left(\mathrm{E}_{\min/\max} \pm \Delta\mathrm{E}\right)\sin\left(\frac{1}{2}\left\{\tan^{-1}\left[\frac{\pm a \pm \delta r + f\,\tan\left(2\theta_{\max/\min} - \phi_{\max/\min}\right)}{f}\right] + \phi\right\}\right)}, \quad (4)$$

where h is the Planck constant and c is the speed of light and ΔE is the energy resolution of the detector at FWHM. The uncertainty in the measurement of the linear distance r is expressed in terms of a minimum detectable increment as $\pm\delta r$, which in practice will be a function of the native "staring" resolution of the snapshot detector.

2.3 Experiment setup

Experiments were conducted using a Hamamatsu microfocus X-ray source with a tungsten target and focal spot size of 40µm; the accelerating voltage and current were 130 kV, 300 µA, respectively. An annular beam with an opening angle, of 3.92° ± 0.05° or $\phi_{\max} = 3.97^{o}$, $\phi_{\min} = 3.87^{\circ}$ was created with the aid of a bespoke tungsten optic. A pinhole aperture of radius a=0.75 mm, in a 3 mm thick lead sheet was placed $A = 400\,mm$ from the X-ray source. Scattered X-rays were detected using a $20\,mm \times 20\,mm \times 1mm$ cadmium telluride (CdTe) pixelated, $250\,\mu m$ pitch, energy resolving detector placed at $D = 500\,mm$ from the X-ray source i.e. $f = 100\,mm$. The energy resolution of the detector, ΔE at FWHM was estimated as $850\,eV$ in our setup. More details about this detector can be found in Seller *et al* (2011) [24]. Three sample materials with different crystallographic textures were placed in the beam together at sample distances described in Table 1. Snapshot images were taken with 10, 5 and 1 second exposures for comparative analysis (and 300 seconds for an enhanced spatial image). The data from each exposure was subject to a background subtraction and Savitzky-Golay filtering using built-in Matlab functions. Reference patterns for each material were obtained from the ICDD database, the card numbers for which are presented in Table 1.

Table 1. Details of the three different sample materials used in the experiments.

Sample material	Thickness (mm)	Source-to-sample mid-plane distance (mm)	Crystallographic texture	ICDD standard card number
Calcite	~15	135	Near NIST standard	00-005-0586
Sodium chloride	~15	185	Large grain size	00-001-0993
Aluminum	8	225	Preferred orientation	00-004-0787

3. Results and discussion

Diffracted flux from the overlapping extended samples, detailed in Table 1, was optically coupled onto the pixelated energy-resolving detector via a centrally positioned 1.5 mm diameter aperture. The energy or equivalently wavelength of incident photons was measured and recorded for each pixel. For illustration purposes a long exposure image collected over 300 seconds is shown in Fig. 2(a) where all detectable incident photons per pixel were summed and color coded according to total count values i.e. an unweighted composite of the different spectral frames recorded. The calcite sample (closest to the source) produced the innermost ring, sodium chloride the middle ring and the aluminum sample (closest to the detector) the outermost ring. Large grains of sodium chloride produced a non-uniform intensity around the corresponding annular image whereas the uniform Debye cone contributions from the calcite and the aluminum provide a relatively smooth intensity distribution. This observation is consistent with studies of large grain size samples in competing EDXRD techniques in which “super peaks” and or the disappearance of peaks were reported as a limiting case for robust material phase identification [25]. The resultant polychromatic spatial image was as predicted by our theory e.g. the dotted arcs in Fig. 2(a) have been plotted according to Eq. (2) using the true sample axial positions stated in Table 1. The material phase signature for each sample are contained within vertical bands when transposed into (d, z) space, see Fig. 2(b), therefore, each column of pixels corresponds to an integrated conic section through an annular gauge volume. Also, the broadening of the calculated d-spacing values, Δd, attributable to the physical system parameters is observable in (d, z) space as an axial spread of the true d-spacing value e.g. the 1.99 Å peak from the sodium chloride sample, via Eq. (5) shown in Fig. 2(b).

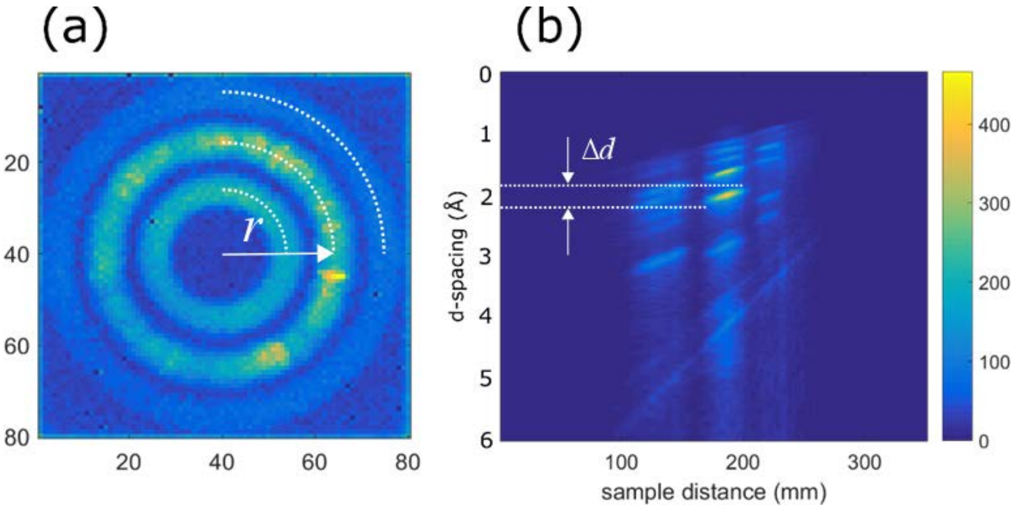

Fig. 2. (a) Integrated intensity image of three normally positioned samples; calcite (innermost ring closest to the source), sodium chloride (middle ring) and aluminum (outermost ring closest to the detector). In this example a relatively long exposure time of 300 seconds (90 mAs) was used to enhance the spatial image. The dotted arcs on radii r have been plotted according to Eq. (3) using the mean true axial sample positions. (b) d-spacing v sample distance (z) representation of the image data, via Eqs. (2)-(3). Systematic broadening, $\Delta d = 0.36$ Å, recorded for the 1.99 Å d-spacing of the sodium chloride sample, via Eq. (4).

The material phase signatures mapped in Fig. 2(b) may be presented as a conventional 1D diffractogram by the simple expedient of plotting d-spacing values following Eq. (3) against sample distance i.e. reducing the dimensionality by discarding axial distance. Thus a composite of d-spacing contributions calculated from successive conic sections through the annular gauge volume may be presented as a single 1D diffractogram. In this way the resultant diffractogram is informed by spectral flux measurements from an increased total number of crystallites providing enhanced particle statistics. For example, representative diffractograms obtained from subsamples of the diffracted flux from sodium chloride can lead to ambiguous or incorrect material phase identification. This finding supports previously reported EDXRD experiments using a single point detector to integrate diffracted flux from extended specimen paths [18].

1D diffraction patterns obtained from the calcite, sodium chloride and aluminum samples positioned together along the primary beam are presented in Figs. 3(a)-3(c), respectively. The results of three different exposure times; 10, 5 and 1 seconds are illustrated for comparative purposes in Fig. 3. The plots have been time normalized and vertically offset for clarity. No *a priori* sample position information was used in the production of the diffractograms.

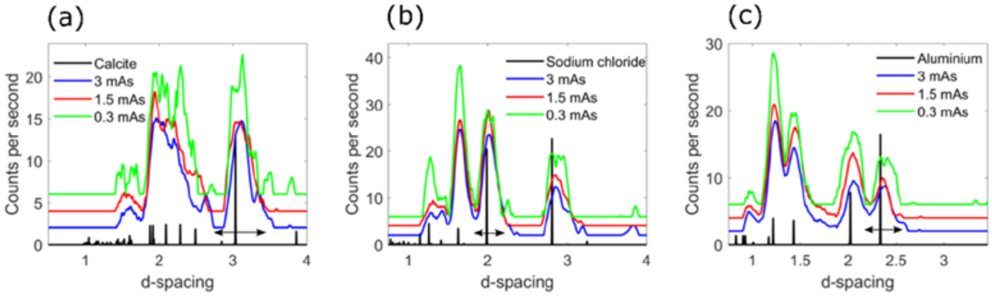

Fig. 3. 1D diffraction patterns for three different samples positioned together in the beam with true source-to-sample separations indicated in parentheses; (a) calcite (135 mm) (b) sodium chloride (185 mm) and (c) aluminum (225 mm). The signals were integrated over exposure times; 3, 1.5 and 0.3 mAs equating to 10, 5 and 1 seconds, respectively. A Savitzky-Golay smoothing filter has been applied. The diffractograms have been time normalized and vertically offset for clarity. Error bars indicate the systematic broadening Δd for principal peaks. The associated true-d-spacing and Δd (Å) values are; (a) 3.035, 0.68 (b) 1.990, 0.36 and (c) 2.388, 0.39, respectively.

The experimental peak positions exhibit good correspondence with the standard peak positions although some degradation between the practical peaks can be observed with decreasing integration time. It is possible to identify the material phase of each sample using a 0.3 mAs snapshot exposure. The peaks exhibit systematic broadening due to the concatenated effects of the physical parameters, which describe the primary/diffracted beam collimation and energy/spatial resolution of the detector. The broadening Δd (Å) was calculated following Eqs. (1)-(4). An example error bar is shown about a principal peak on each diffractogram in Fig. 3. The associated true d-spacing and Δd (Å) values are; (a) 3.035, 0.68 (b) 1.990, 0.36 and (c) 2.388, 0.39, respectively. This analysis assumes that the spot size of the X-ray source, 40 μm, is negligible. The size of the pinhole aperture, $a = 0.75\,mm$ was the dominant parameter for systematic broadening in our setup. For example, the value of Δd (Å) is approximately halved by setting $\Delta E = 0$ and $\delta r = 0$. The effect of angular uncertainty upon energy dispersive transmission measurements was anticipated and is well understood [26]. The scattering patterns from closely spaced or multiphase samples may also be a combination of the different components (crystalline and non-crystalline) present in the samples. Resultant diffractograms approximate the linear sum of scattering from each individual component weighted by the relative mass and scattering power. In our experiment geometric unsharpness of around $3\,cm$ over the axial range of the system was calculated from consideration of Eqs. (1)-(4). This calculated value is consistent with the experiment results observed in Fig. 2. It is routine in diffraction laboratories to quantify the phase composition of mixtures even when one of the components is amorphous [27,28]. If crystalline materials are very closely spaced in the object, then the single diffractogram measured would contain Bragg peaks from all materials simultaneously. Phase identification from mixed materials is also a problem that has several potential solution strategies that are adopted routinely within diffraction laboratories [29,30]. These methods may be applied to the diffractograms produced by our technique. Thus the likelihood of being able to distinguish or identify very closely spaced materials is high given the appropriate treatment of the raw data. The ability to discriminate the components in a mixed material phase is particularly relevant in security screening and is a driver for our ongoing effort. The ill-defined shape and random alignment of samples in a bag or suitcase are encountered routinely at security checkpoints. The intrinsic characteristic of our diffraction probe enables the analysis of the spatial distribution of diffracted flux from a succession of annular specimen paths. We anticipate that the automated segmentation of specimen paths to identify crosscutting and or partial 'threat sample planes' to be an important area for ongoing investigation. However, before conducting a more systematic and rigorous study we will design and construct a system optimized for security screening applications.

4. Conclusions and future work

We have demonstrated material phase identification of three overlapping samples via a single conical shell X-ray exposure or snapshot. The diffracted flux from the central dark field was collected using a pinhole aperture optically coupled to a pixelated energy resolving detector employing exposure times down to 0.3 mAs. No *a priori* knowledge of the sample's position was required in the calculation of d-spacing values. This direct detection method [4] demonstrates that there is a one-to-one correspondence between photon counts and exposure time.

The relatively low power, 39 W (130 kV, 300 µA) of the X-ray generator in comparison to those used in other studies [5,6, 12–15] supports the working hypothesis that by exploiting a brighter X-ray source our method should approach real-time operational speeds. Our imaging architecture would then be of great benefit to fields requiring high-speed materials identification from spatially distributed objects such as security screening, process control and diagnostic imaging. Future work will focus on scanning implementations of this architecture to generate true 4D i.e. volume and material phase reconstructions together with alternate encoding masks to increase sensitivity.

Funding

Department of Homeland Security, Science and Technology Directorate, Homeland Security Advanced Research Projects Agency, Explosives Division through the Advanced X-ray Material Discrimination Program; contract HSHQDC-15-C-B0036.